

Carbonic Anhydrase-Mimicking Supramolecular Nanoassemblies for Developing Carbon Capture Membranes

Somaye Nilouyal, H. Enis Karahan, Ali Pournaghshband Isfahani, Daisuke Yamaguchi, Andrew H. Gibbons, Masateru M. M. Ito, Easan Sivaniah,* and Behnam Ghalei*



Cite This: *ACS Appl. Mater. Interfaces* 2022, 14, 37595–37607



Read Online

ACCESS |

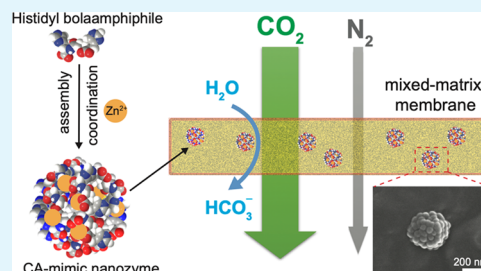
Metrics & More

Article Recommendations

Supporting Information

ABSTRACT: As a ubiquitous family of enzymes with high performance in converting carbon dioxide (CO_2) into bicarbonate, carbonic anhydrases (CAs) sparked enormous attention for carbon capture. Nevertheless, the high cost and operational instability of CAs hamper their practical relevance, and the utility of CAs is mainly limited to aqueous applications where CO_2 -to-bicarbonate conversion is possible. Taking advantage of the chemical motif that endows CA-like active sites (metal-coordinated histidine), here we introduce a new line of high-performance gas separation membranes with CO_2 -philic behavior. We first self-assembled a histidine-based bolaamphiphile (His-Bola) molecule in the aqueous phase and coordinated the resulting entities with divalent zinc. Optimizing the supramolecular synthesis conditions ensured that the resultant nanoparticles (His-NPs) exhibit high CO_2 affinity and catalytic activity. We then exploited the His-NPs as nanofillers to enhance the separation performance of Pebax MH 1657. The hydrogen-bonding interactions allowed the dispersion of His-NPs within the polymer matrix uniformly, as confirmed by microscopic, spectroscopic, and thermal analyses. The imidazole and amine functionalities of His-NPs enhanced the solubility of CO_2 molecules in the polymer matrix. The CA-mimic active sites of His-NPs nanozymes, on the other hand, catalyzed the reversible hydration of CO_2 molecules in humid conditions, facilitating their transport across the membranes. The resulting nanocomposite membranes displayed excellent CO_2 separation performance, with a high level of stability. At a filling ratio as low as 3 wt %, we achieved a CO_2 permeability of >145 Barrer and a CO_2/N_2 selectivity of >95 with retained performance under humid continuous gas feeds. The bio-inspired approach presented in this work offers a promising platform for designing durable and highly selective CO_2 capture membranes.

KEYWORDS: carbon dioxide, membrane technology, bolaamphiphiles, self-assembly, nanozyme



1. INTRODUCTION

The ever-growing human population and urbanization cause immense pressure on environmental health, necessitating the urgent development of greener processes for energy production.¹ Ambitious targets such as a renewables-driven hydrogen economy are very appealing in the long run.² But concerted efforts should also be devoted to minimizing the carbon footprint of currently employed energy generation technologies.³ To this end, it is vital to mitigate the carbon dioxide (CO_2) emissions at power stations.⁴ Compared to traditional CO_2 capture technologies, such as chemical absorption, physical adsorption, and cryogenic distillation, membrane-based gas separation processes are more promising to fulfill this need with their low energy consumption, small device footprints, practicality in operation, and customizability.⁵ However, currently available membrane materials suffer from poor operational stability and a trade-off between permeability and selectivity, thus failing to meet the industrial requirements.⁶

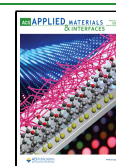
The recent efforts to design industrially appealing CO_2 capture membranes with high durability and selectivity have primarily focused on manipulating the microenvironment of

CO_2 transport pathways through physical and/or chemical means.⁷ The physical approach involves enhancing the diffusion of CO_2 molecules by optimizing the size, distribution, and tortuosity of the transport channels,⁸ whereas the tuning of the chemical microenvironments mainly aims at improving the structural stability,⁹ solubility,¹⁰ and facilitating the transport of CO_2 .¹¹ As an example of the chemical approach, facilitated transport membranes are particularly interesting where the reversible reactions and complexation of CO_2 molecules with carriers boost their permeation, while other gases pass through the membranes by solution-diffusion mechanism.¹² As a result, facilitated transport membranes can deliver high CO_2 permeability and CO_2 selectivity over relatively inert gases such as N_2 , CH_4 , and H_2 .¹³

Received: April 10, 2022

Accepted: August 2, 2022

Published: August 15, 2022



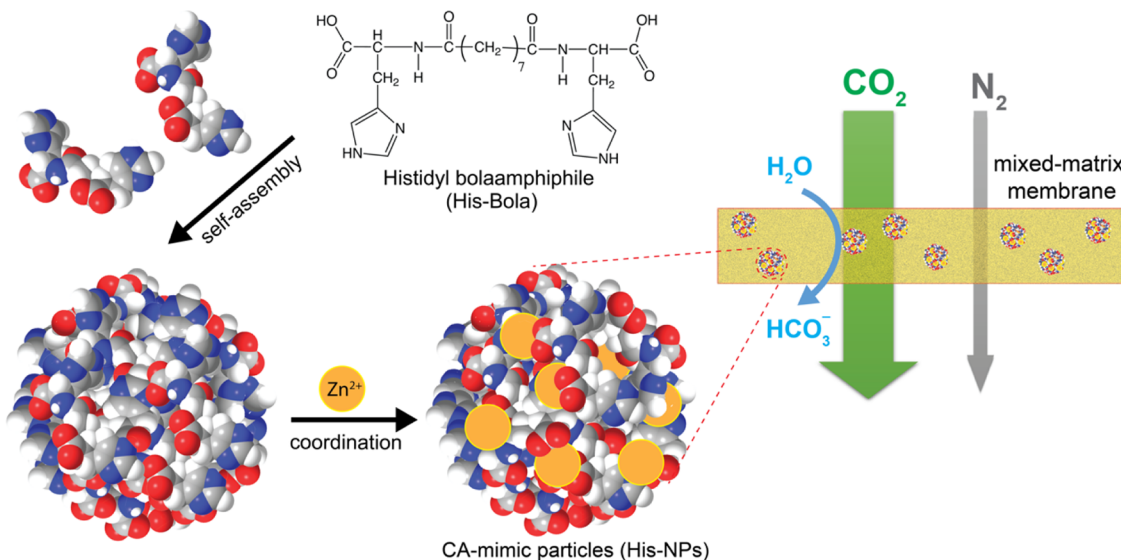


Figure 1. Schematic illustration of CA-mimic-based nanocomposite membranes for CO_2 separation. Carbon, oxygen, and nitrogen atoms are shown in gray, blue, and red, respectively. Orange circles represent zinc ions.

With its exceptional CO_2 affinity, the carbonic anhydrase (CA) enzymes have been used as a carrier to design CO_2/N_2 separation membranes by following different strategies.^{14,15} However, it is challenging to obtain CA affordably at a purity level suitable for membrane fabrication.¹⁶ Furthermore, enzymatic membranes containing bio-origin CA are vulnerable to thermal deactivation, short lifetime, and pH sensitivity.¹⁷ The immobilization of CA to organic, inorganic, and hybrid microparticles offers a possible solution to these problems.¹⁸ But immobilization techniques are not free of obstacles as they are usually prone to enzyme leakage and subsequent activity loss.¹⁹ To work around these issues, synthetic materials with CO_2 affinity, such as organometallics,^{20,21} metal-coordinated porous polymers,²² and metal-organic frameworks,²³ have been designed and utilized as CA-mimicking fillers for membrane fabrication. These synthetic systems, however, lack amino acid content and are not formed by supramolecular interactions, thus differing substantially from native CAs. Hence, in this study, we explored the design of a new line of nanozymes with remarkable chemical similarity to the active site of CAs. Furthermore, compared with other reported CA mimics, the organic and amorphous structure of these nanozymes make them highly compatible with polymer matrices, even at high loadings, for developing efficient CO_2 capture membranes.

Here, we report the designing of a high-performance CO_2 capture membrane enabled by CA-mimicking supramolecular nanoparticles. In our membrane design, zinc-bound histidine-containing bolaamphiphilic assemblies (His-NP nanozymes), which resemble the active site of CAs, served as the transport facilitating agent (nanofiller) (Figure 1). And a commercially available poly(ether-block-amide) was employed as the matrix element of the resulting mixed-matrix membrane (MMM) structure. The organic groups existing in the nanofiller structure, such as carboxyls, imidazoles, and amines, elevate the solubility of CO_2 in the membrane structure. Also crucially, similar to the activity of natural CA enzymes, the His-based enzyme-mimic nanoparticles (His-NP nanozymes) catalyze the hydration of CO_2 in the presence of water, facilitating CO_2 transport through the polymer film. On top, the CA-mimic particles have higher thermal stability than CA enzymes (above 250 °C), making the

developed membrane structures potentially more suitable for industrial operations. Thus overall, the biomimetic membranes delivered in this work offer a cost-effective and durable platform for realizing highly efficient CO_2 separation from humid-gas streams of industrial relevance.

2. EXPERIMENTAL SECTION

2.1. Materials. Pebax MH 1657 (Pebax) pellets were purchased from Arkema, France. L-histidine monohydrochloride monohydrate (98%), para-toluene sulfonic acid monohydrate, azelaic acid (98%), N-hydroxysuccinimide (NHS, 98%), 1,1,3,3-tetramethyluronium hexafluorophosphate (HBTU, 98%), and para-nitrophenol (*p*NP, 99%) were obtained from Sigma-Aldrich. Benzyl alcohol (99%), *N,N*-diisopropylethylamine (DIEA, 99%), and para-nitrophenyl acetate (*p*NPA) were supplied by TCI Chemicals. The solvents, *i.e.*, ethanol (99%), acetone (99%), diethyl ether (super dry), *N,N*-dimethylformamide (DMF, super dry), chloroform (super dry), and acetonitrile (super dry), were purchased from Wako Pure Chemical Industries. All of the chemicals were used as received.

2.2. Bolaamphiphile Synthesis. L-histidine benzyl ester *para*-toluenesulfonate was synthesized according to the previous report by reacting L-histidine monohydrochloride monohydrate and *para*-toluenesulphonic acid monohydrate in benzyl alcohol media.²⁴ L-histidine benzyl ester *para*-toluenesulfonate was reacted with azelaic acid following carbodiimide conjugation protocol to produce the bolaamphiphile histidine compound (His-Bola).²⁵ Briefly, 6 g of azelaic acid and 12 g of HBTU were dissolved in 1 L of DMF. Then, 20 g of L-histidine benzyl ester *para*-toluenesulfonate, 3.4 g of DIEA, and 3 g of NHS were added to the reaction mixture. The mixture was kept at 4 °C for 16 h under stirring to complete the conjugation reaction. Using a rotary evaporator, the solvent was removed at 40 °C, and the intermediate ester compound was precipitated in ethanol. His-Bola was obtained by base hydrolysis of the intermediate compound at 75 °C for 6 h. The final product was washed with diethyl ether several times and precipitated in acetone.

2.3. Supramolecular Nanozyme Synthesis. We dissolved the purified His-Bola precursor in pH-controlled (pH ~7) deionized water to prepare a 10 mM solution. The His-Bola solution was bath-sonicated for 15 min (at 0 °C global temperature), stirred for 1 h, and then mixed with a certain amount of ZnCl_2 aqueous solution to form supramolecular nanozymes. The mixture was stirred at room temperature for 6 h to ensure the completion of the coordination reaction. The molar ratio of Zn^{2+} to His-Bola was adjusted to 0, 0.001, 0.01, and 0.1.

2.4. Membrane Fabrication. Solution casting and solvent evaporation techniques were used to fabricate neat Pebax membranes and nanocomposites (MMMs). The casting solutions were prepared using 4 wt % Pebax solution with a certain amount of His-NPs in ethanol/water 70/30 v/v %, if any. The solutions were sonicated for 2 h and stirred for 24 h before use. The filler loading ratios were kept in the range of 0–9 wt % with respect to the total mass of the membranes. Five milliliters of each solution was cast on a Teflon petri dish, dried at 40 °C for 1 day, followed by 12 h vacuum drying at 70 °C before the measurements. The average thicknesses of the prepared membranes were ~70 μm, as measured by a micrometer caliper (MDC-50MX, Mitutoyo, Japan).

2.5. Characterization Methods. We measured ¹H NMR spectra in deuterated dimethyl sulfoxide (DMSO-*d*₆) using a Bruker 500 MHz spectrometer. The Fourier transform infrared (FTIR) spectra of neat Pebax, freeze-dried His-NPs, and their composites were collected in the range of 4000–800 cm⁻¹ with a resolution of 2 cm⁻¹ and 256 scans using an IRTracer-100 spectrometer (Shimadzu, Japan). The crystalline structure of the freeze-dried fillers and membranes was tested by X-ray diffraction (XRD) (Rigaku RINT XRD, Japan) in the range of 5–40° at the scan rate of 2° per min using Cu Kα radiation under a voltage of 40 kV and a current of 200 mA. A dynamic light scattering (DLS) instrument (DLS-8000/6500, Otsuka, Japan) was used to obtain the intensity-averaged hydrodynamic size distribution of His-NPs (at a detector angle of 90°). X-ray photoelectron spectroscopy (XPS, ULVAC-PHIMT-5500, Japan) instrument using Mg Kα (1254.0 eV) as radiation source (the takeoff angle of the photoelectron was set at 90°) was used to analyze the surface chemical structure of freeze-dried His-Bola assemblies and His-NP structures. Survey spectra were collected over a range of 0–1100 eV, and high-resolution spectra of C 1s, N 1s, and O 1s peaks were also collected. The melting (*T*_m) and glass transition (*T*_g) temperatures of freeze-dried particles and membranes were measured using a differential scanning calorimeter (DSC, 60 Plus, Shimadzu, Japan) under a nitrogen atmosphere in the range of –80–250 °C with a 10 °C per min scanning rate. Initially, the samples were heated to 80 °C to remove the thermal history. The degree of crystallinity (*X*_c) of poly(ethylene oxide) (PEO) and polyamide 6 (PA-6) phases were calculated from the area under the endothermic peaks in DSC thermograms as follows

$$X_c (\%) = \frac{\Delta H_m}{\Delta H_0} \times 100 \quad (1)$$

where ΔH_m (J g⁻¹) is the melting enthalpy of each crystalline phase, and ΔH_0 (J g⁻¹) is the enthalpy of melting of either pure crystalline PEO or PA-6 (166.4 and 230 J g⁻¹ for PEO and PA-6, respectively).²⁶ The total crystallinity of the membranes was derived considering the ratio of PEO/PA-6 (60/40 wt %) in Pebax and its amount in the samples.

Thermogravimetric analysis (TGA, Rigaku Thermo plus EVO2) was employed under a nitrogen atmosphere at a heating rate of 10 °C per min to evaluate the thermal stability of the fillers and membranes. The membrane morphologies were observed by FESEM (JEOL, JSM-7500F). To observe the cross-section of the membranes, the samples were freeze-fractured in liquid nitrogen and coated with osmium to prevent charging. The phase behaviors of the membranes were also analyzed using atomic force microscopy (AFM, NanoWizard III, JPK Instruments) in tapping mode.

The nanomechanical properties of the neat Pebax and representative MMMs were performed using a nanoindentation tester (ENT 2100, Elionix) equipped with a Berkovich three-sided pyramid diamond tip (radius of 100 nm) with a load of 1 mN. Each indent was made in the samples up to a maximum depth of around 2 μm. Twenty points in a rectangular configuration were tested on each sample; the average data were calculated based on the measured values of three different samples.

2.6. Catalytic Activity Assessment. The catalytic activity of the His-NP particles was assessed from the *p*NPA (substrate) hydrolysis reaction.²⁷ The kinetic rate of hydrolysis reaction was analyzed by calorimetric evaluation of the formation of *p*NP (product) using ultraviolet-visible (UV-vis) spectroscopy (Shimadzu UV-1800) with

a predetermined calibration curve. The aqueous His-Bola assemblies coordinated with Zn²⁺ (500 μL) were mixed with a *p*NPA solution in acetonitrile (5 μL) in a plastic UV cuvette (UVette, Eppendorf). We then tracked the hydrolysis of *p*NPA in time by recording the optical absorbance at 400 nm and fixing the pH at 7 (~25 °C). The substrate concentration was in the range of 0.2–4 mM. Michaelis–Menten model was fitted to the kinetic data to calculate the kinetic parameters (see the Supporting Information for further details on catalytic activity measurements.)

The pH stability of His-NPs was examined by testing their ability to retain catalytic activity at different pH values. We adjusted the pH of aqueous His-NP solutions to 4, 7, and 10 and kept them under stirring for 24 h. We then fixed the pH at 7 to eliminate the direct effect of pH on *p*NPA (1 mM) hydrolysis and tracked the response by recording the optical absorbance at 400 nm (~25 °C).

2.7. Gas Transport Measurements. Pure gas permeabilities of the membranes were determined by the constant volume-variable pressure method at ~25 °C. Millipore high-pressure filter holder (XX4502500) was used to seal the membranes for the measurements. The gas permeate pressure was recorded by a pressure transmitter (Keller PAA 33X).

The gas permeability (*P*) is calculated based on the following equation

$$P = \frac{Vl}{A p_f p_0 T} \left(\frac{dp}{dt} \right) \quad (2)$$

where *P* is the gas permeability, in Barrer (1 Barrer = 10⁻¹⁰ cm³(STP)cm cm⁻² s⁻¹cm Hg⁻¹), *V* is the permeate volume (cm³), *l* is the membrane thickness (cm), *A* is the effective membrane area (cm²), *p*_f is the feed pressure (cmHg), *p*₀ is the pressure at standard state (76 cmHg), *T* is the absolute operating temperature (K), *T*₀ is the temperature at standard state (273.15 K), and (dp/dt) is the slope of pressure increase in the permeate volume at pseudo-steady state (cmHg s⁻¹).

The ideal selectivity (*α*) of gas pairs, *A* and *B*, is defined as

$$\alpha_{A/B} = \frac{P_A}{P_B} \quad (3)$$

The diffusion coefficient (*D*) for each gas is derived by following eq 4, using the membrane thickness and time lag(*θ*)

$$D = \frac{l^2}{6\theta} \quad (4)$$

The solubility coefficients (*S*) are calculated according to eq 5

$$S = \frac{P}{D} \quad (5)$$

The feed side pressure of the gas was 2 bar at single-gas measurements. Permeability coefficients were calculated three times for each membrane, and the average data was reported. The error for the absolute values of the permeability coefficients was about ±7% due to uncertainties in determining the gas flux and membrane thickness.

The mixed-gas permeation was measured using the constant pressure-variable volume method. The membrane was exposed to CO₂/N₂ (15/85 vol %, Kyoto Teisan, Japan) mixed gas with feed pressure between 2–8 bar at room temperature (25 °C). The volumetric flow rates of feed gas were kept at 100 mL min⁻¹ by a digital mass flow controller (Horiba). Helium was used as the sweep gas at a volumetric flow rate of 50 mL min⁻¹. The permeability and compositions of permeate gas mixtures were measured by an in-line gas chromatograph (Shimadzu, model 2014) equipped with a thermal conductivity detector (TCD). For the humid-gas tests, the feed gas was humidified by a gas bubbler filled with saturated solutions of LiCl (12% relative humidity (RH)), MgCl₂ (33% RH), and water (85% RH), and RH values were recorded with a humidity sensor (Honeywell HIH-4000) before the gas measurements.

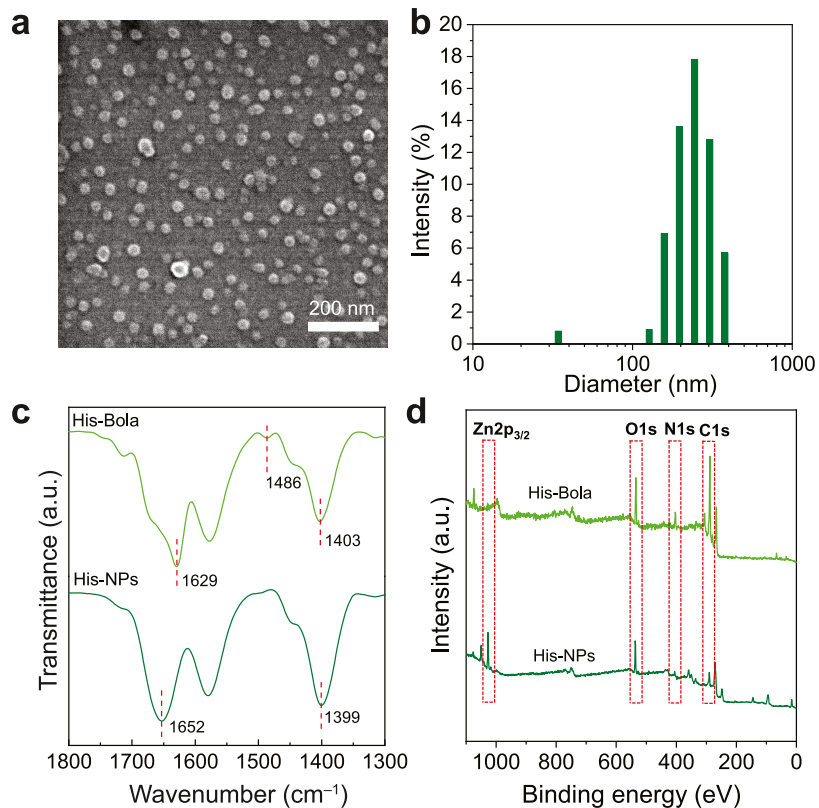


Figure 2. (a) FESEM image of His-NPs on the surface of a silicon wafer, (b) DLS analysis of His-NPs, (c) FTIR spectra of freeze-dried His-Bola and His-NP particles, and (d) survey scan XPS spectra of freeze-dried His-Bola and His-NP.

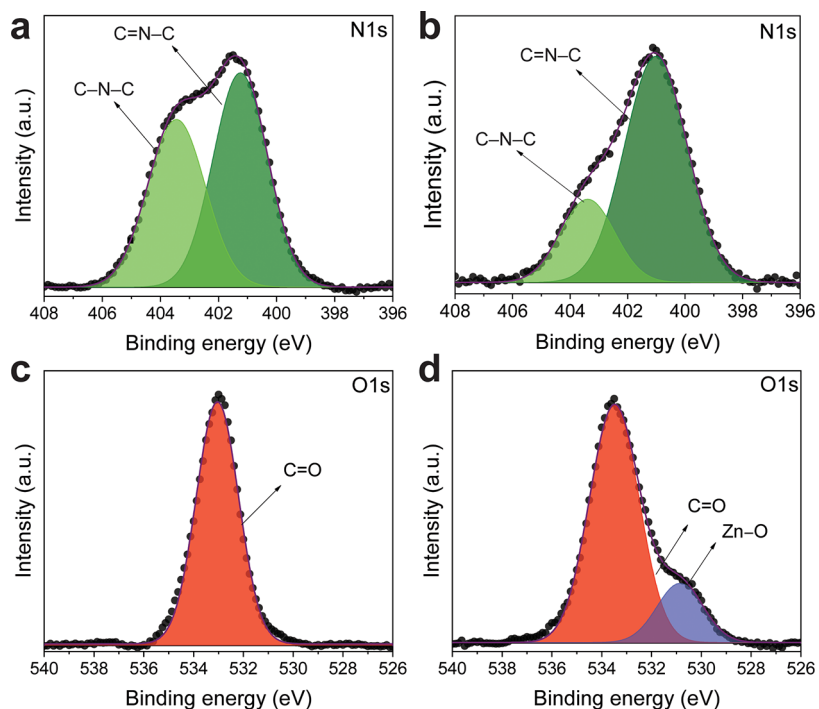


Figure 3. High-resolution XPS spectra of freeze-dried His-Bola and His-NP nanozymes: N 1s of (a) His-Bola and (b) His-NPs; O 1s of (c) His-Bola and (d) His-NPs.

3. RESULTS AND DISCUSSION

3.1. His-NPs Nanoparticles Characterization and Catalytic Activity.

¹H NMR confirmed the successful synthesis of His-Bola *via* the conjugation of azelaic acid and histidine

benzyl ester (Figure S1). Zn²⁺-coordinated particles (His-NPs) formed globular assemblies of 20–50 nm on the solid surface (Figure 2a). Supposedly due to the aggregation of these primary particles, the DLS study showed that the resultant His-NPs

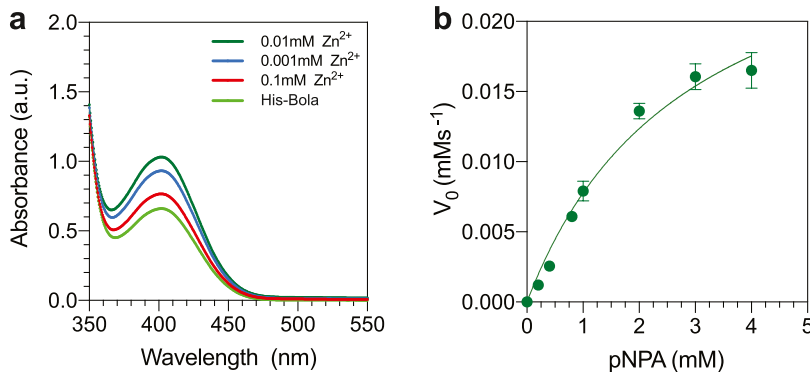


Figure 4. (a) UV–vis spectra of His-Bola assembly and His-Bola assemblies coordinated with Zn²⁺ at various concentrations in the presence of pNPA and (b) initial hydrolysis rate (V_0) of His-NPs at different concentrations of pNPA.

colloids (10 mM mL⁻¹) also abundantly contain larger particles with an average size of ~250 nm (Figure 2b). The DLS data indicates no marked difference between the size distributions of His-Bola assemblies and metal-coordinated nanoparticles (His-NPs). This is probably due to the low concentration of Zn²⁺ (0.01 mM) in the solution (Figure S2). As we verified with FTIR spectroscopy, His-Bola molecules are successfully coordinated with Zn²⁺ ions in His-NPs (Figure 2c). The peak denoting the imidazole ring stretching (at 1486 cm⁻¹) in His-Bola samples disappeared upon Zn²⁺ coordination. In addition, the carboxylic group peaks of the His-Bola structure are displaced in the presence of Zn²⁺ ions. In particular, the peak corresponding to the symmetric stretching of the carboxyl groups at 1403 cm⁻¹ slightly moved toward a lower wavenumber (1399 cm⁻¹) in Zn²⁺-coordinated particles.²⁸

Generally, the carbonyl stretching vibrations are highly susceptible to their local chemical and electrostatic environment. The positively charged Zn²⁺ ions pull the carbonyl bonds' electron density away and reduce the vibration frequency.²⁹ Besides, the asymmetric stretching peak of the carboxyl groups blue-shifted to 1652 from 1629 cm⁻¹. These shifts suggest that His-Bola assemblies are coordinated with Zn²⁺ ions through carboxylic and imidazole moieties.

We further confirmed the inclusion of Zn atoms in the His-NP structures by XPS analysis (Figure 2d). The XPS spectra of His-Bola and His-NP samples showed peaks attributable to oxygen (O 1s at ~533 eV), nitrogen (N 1s at ~400 eV), and carbon (C 1s at ~285 eV), and His-NPs also contained an additional peak at ~1025 eV corresponding zinc species (Zn 2p). Figures S3 and 3 presented the binding energies of the C 1s, N 1s, and O 1s electrons of His-Bola assemblies and His-NPs. The C 1s spectrum of His-NPs shows peaks at 284.8, 286.7, and 289.3 eV, which are attributed to C–C, C–N/C–O, and C=O bonds, respectively. The water-induced self-assembly of bolaamphiphiles naturally pushes the hydrophilic tails outward (toward the aqueous environment);³⁰ thus, the outer shells of the resulting aggregates are expected to be rich in packed histidine imidazole and carboxylic moieties. This expectation is in agreement with the XPS observation, where the intensity of C–N/C–O and C=O components are remarkably higher than the intensity of C–C components on the surfaces of His-NPs (Figure S3).

We further compared the deconvoluted N 1s and O 1s XPS spectra of His-Bola and His-NPs to assess the effect of Zn²⁺ coordination on the chemical structure of the His-NP nanofillers. There are two strong features at 401.1 and 403.4 eV related to C=N–C (imino) and C–N–C (amino) nitrogen atoms of His-Bola molecules,³¹ respectively (Figure 3a). After

coordination with Zn²⁺, the intensity of amino nitrogen peak is reduced in His-NPs, while the peak related to imine nitrogen becomes broader (Figure 3b), confirming the interactions of Zn²⁺ ions with amine groups. Generally, amines are more basic than imines (higher pK_a values), so they contribute to metal-coordination reactions more. And, coordination with Zn²⁺ might disturb the intermolecular hydrogen-bonding interactions, shifting the binding energy of amino N 1s toward the lower levels. The O 1s spectrum of His-Bola shows a single peak at 533.2 eV (Figure 3c), which implies the presence of carboxylic groups. Additionally, the absence of peaks related to hydroxyl forms of oxygen suggests the deprotonation of carboxylic groups during the formation of His-Bola assemblies. A new peak appears in the O 1s spectrum of His-NPs at 530.8 eV following the coordination with Zn²⁺ due to the generation of Zn–O coordination bonds³² (Figure 3d).

In addition, incorporating Zn²⁺ into His-NPs enhanced their thermal stability (above 250 °C), leaving more residues compared to His-Bola, possibly due to the formation of pyrolyzed zinc complexes, at temperatures up to 500 °C (Figure S4). As we have evidenced above, these Zn-bound sites are highly populated at the outer shells of the surface functional groups of His-Bola assemblies, forming active catalytic sites that mimic the architecture of metalloenzymes. We, therefore, assessed the catalytic activity of the His-NPs by deacetylation of pNPA substrate, which follows a mechanism similar to CO₂ hydration.³³

For evaluating the CA-mimicking capacity of His-NPs, we initially tested the effect of Zn²⁺ concentration on the catalytic activity to find the optimal condition for coordination. His-NPs catalyze the hydrolytic conversion of pNPA to pNP, which turns the transparent solution into yellow and can be monitored by a change in optical absorbance at 400 nm. As shown in Figure 4a, at constant concentrations of His-Bola (10 mM) and substrate (1 mM), the amount of produced pNP varies with the Zn²⁺ content of His-NPs. In particular, we observed higher catalytic activity and thus higher product concentration and optical absorbance in the His-NPs made with 0.01 mM. Therefore, these particles were selected as fillers for developing the MMMs. Figure 4b illustrates the initial hydrolysis rate (V_0) of His-NPs at pH 7 and 25 °C for various substrate concentrations. Afterward, the Michaelis–Menten model was fitted to the data to calculate the kinetic parameters. (Table S1 in the Supporting Information summarizes the kinetic parameters derived from Figure 4b.) Additionally, we evaluated the catalytic efficiency of His-NPs for CO₂ hydration under continuous CO₂ gas exposure in an aqueous solution (Figure S5). Notably, in the presence of His-

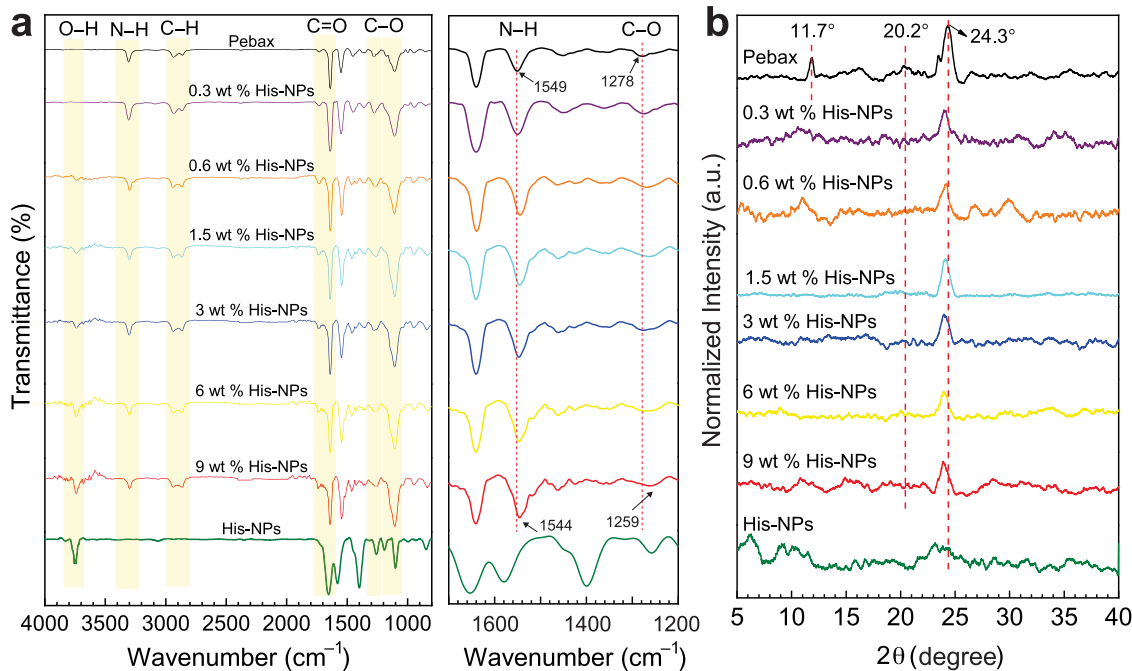


Figure 5. (a) FTIR spectra and (b) XRD patterns of neat Pebax and His-NPs-based MMMs.

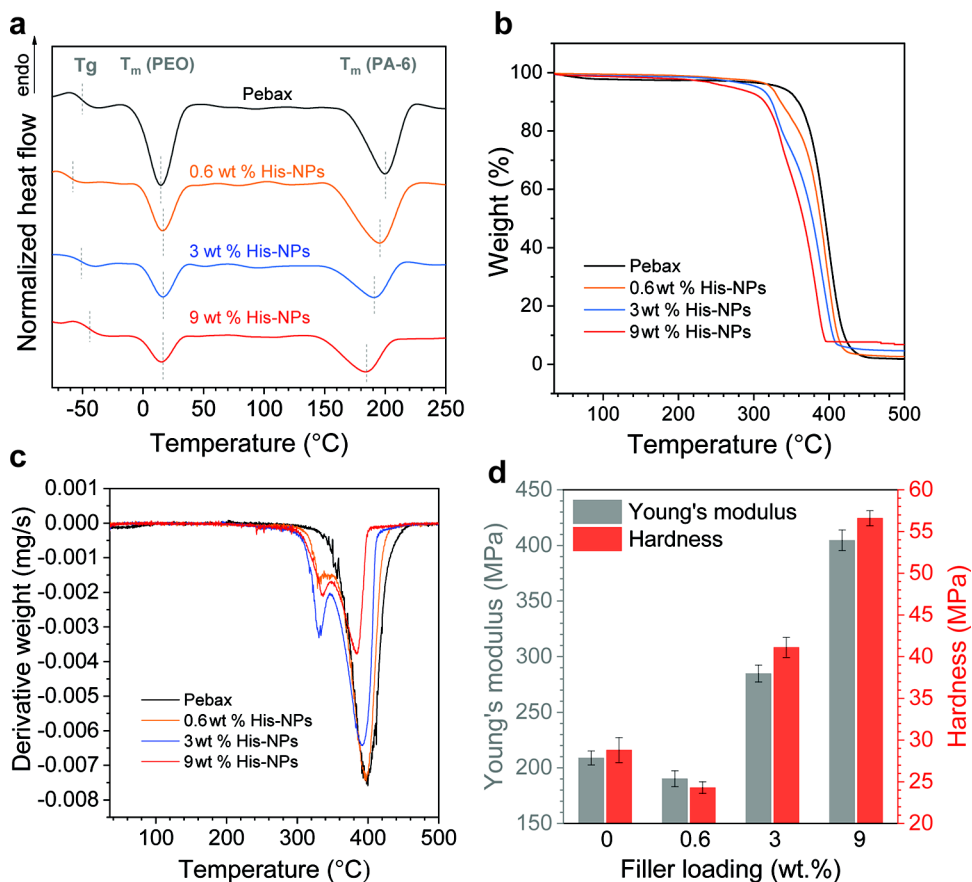


Figure 6. Thermal behavior of neat and nanocomposite membranes based on (a) DSC, (b) TGA, and (c) DTG analyses, and (d) nanoindentation-based mechanical testing of Pebax-based membranes as a function of the His-NP loading. Error bars represent the standard deviation of 20 indents.

NPs, the pH drop was faster than in His-NP-free solution. His-NPs accelerate the conversion of CO₂ into bicarbonate and release more protons, resulting in a further decrease in pH over time. This observation further proves that His-NPs could

efficiently catalyze the CO₂ hydration reaction, confirming their CA-mimicking capacity.

Furthermore, we tested the pH stability of His-NPs by determining their ability to catalyze the hydrolysis of *p*NPA to

Table 1. Thermal Properties Summary of Neat Pebax and Pebax/His-NP MMMs

membranes	T_g (°C)	T_m (°C)		ΔH_m (J g ⁻¹)		X_c (%)			total
		PEO	PA-6	PEO	PA-6	PEO	PA-6	PEO	
Pebax	-51.4	14.9	200.3	20.8	26.1	12.5	11.3	12	
0.6 wt % His-NPs	-57.8	16.7	195.7	15.7	20.6	9.4	8.9	9.1	
3 wt % His-NPs	-50.9	16.7	190.2	10.4	15.3	6.3	6.6	6.2	
9 wt % His-NPs	-43.8	16.5	184.1	9.9	13.8	6	6	5.5	

*p*NP at a wide pH range of 4–10 (Figure S6). These tests suggested that the particles could retain their catalytic activity under both basic and acidic conditions. Considering that the pH of CO₂-saturated water is above 4 (at 1 bar and 25 °C),³⁴ the synthesized His-NP particles possess sufficient pH stability for developing robust CO₂ capture membranes.

3.2. Physicochemical Analyses. We thoroughly investigated the physicochemical effects of incorporating His-NPs into the Pebax matrix at different loadings *via* FTIR (Figure 5a). The neat Pebax film shows several characteristic peaks at 1106 and 1278 cm⁻¹ associated with the O–C stretching in the soft segment (PEO), as well as peaks at 1549, 1640, 1726, and 3307 cm⁻¹ related to N–H bending, C=O stretching (HNC=O and O=C=O), and N–H stretching vibrations in the hard segment (PA-6); the peak at 2866 cm⁻¹ corresponds to C–H stretching of methylene groups in the soft and hard parts,³⁵ respectively. For His-NPs, the peaks observed at 1581 and 1400 cm⁻¹ are attributed to the symmetric and asymmetric stretching of the carboxylate groups, respectively. The stretching of the imidazole ring in His-Bola at 1486 cm⁻¹ diminished after Zn²⁺ coordination to form His-NPs. His-NPs also display a sharp band around 3700 cm⁻¹ due to the O–H stretching vibrations of the adsorbed water, which is evident in the membranes with higher loadings of His-NP fillers. The films comprising His-NPs generally show similar bands as neat Pebax, the major component of the nanocomposite membranes. However, there were some shifts in the spectral features due to its interactions with His-NPs. Upon adding the His-NPs, the N–H stretching and N–H bending bands slightly moved toward lower wavenumbers of 3299 and 1544 cm⁻¹, respectively. These changes occur because of the disruption of the interchain interactions in the hard domains of Pebax and the formation of new hydrogen-bonding interactions between His-NPs and PA-6 chains.³⁶

The intermolecular interactions between the hydrogen atoms on the imidazolium ring, carboxyl and amine groups of His-NPs, and the oxygen atoms of PEO chains could be explored through the changes of the O–C stretching band (at ~1278 cm⁻¹), which has a notable impact on PEO crystallization. A red shifting in the characteristic peak of C–O bond is observed upon adding His-NPs into the Pebax matrix, indicating the formation of hydrogen-bonding interactions between the PEO domains and His-NPs.³⁷ The interaction between His-NPs' functional groups and the Pebax backbone could improve the dispersion of the filler within the polymer matrix and reduce the overall crystallinity of the resulting membranes.

XRD analysis of Pebax, His-NPs, and the MMMs with different loadings was performed at room temperature to characterize their nanostructures and the effect of nanofillers on the crystallinity of the polymer matrix (Figure 5b). The XRD pattern of neat Pebax showed three primary reflection peaks at 11.7, 20.2, and 24.3°. The peak at 11.7° is related to the (002) crystal plane of the PA-6 γ -phase, and the diffraction peak located at 20.2° is assigned to the (020) and (200) reflections of

the PA-6 γ -phase crystals.³⁸ The peak at an angular position of 24.3° is associated with the α -phase crystalline form of PA-6 domains.³⁹ On the other hand, PEO crystalline features were not observed on the XRD patterns of the neat Pebax as the soft segments melt below 25 °C (see DSC data below, Figure 6a). The presence of a broad peak at 20–25° confirms the amorphous character of His-NPs. Adding His-NPs into the Pebax matrix decreased the intensity and shifted the reflection peak maximum to 24.3°, indicating the reduced crystallinity and packing of the polymer phase in MMMs compared to neat Pebax. For example, the diffraction peak shifted from 24.3° (*d*-spacing: 3.6 Å) to 23.9° (*d*-spacing: 3.7 Å) for the sample with 9 wt % His-NPs nanofillers with ~26% lower intensity. Furthermore, the peaks related to the γ -phase of PA-6 domains were diminished in the nanocomposite membranes, suggesting that the interchain hydrogen-bonding in Pebax hard segment is considerably disrupted by the incorporation of His-NPs, as discussed in the FTIR section.

3.3. Thermal and Mechanical Characteristics of the Membranes. Adding functional fillers to semicrystalline polymers might change their crystallinity, chain rigidity, and subsequently, gas transport behavior, altering their thermal transitions.⁴⁰ So, we analyzed the effect of His-NPs on the phase behavior and thermal properties of the nanocomposite membranes, as shown in the DSC and TGA thermograms of Pebax and Pebax/His-NP MMMs, presented in Figure 6a and Table 1, respectively.

DSC thermogram of neat Pebax shows the typical melting transitions of PEO (at 14.9 °C) and PA-6 (at 200.3 °C) crystalline phases with a low T_g of PEO soft domains at -51.4 °C. Thus, the incorporation of His-NPs substantially affected the crystallinity of the Pebax matrix, suggesting the existence of intermolecular interactions between polymer chains and nanoparticles, in agreement with the FTIR results summarized above.⁴¹

In general, an increase in the filler loading caused the broadening and intensity reduction in the melting peaks and decreased melting enthalpy (ΔH_m) of PEO and PA-6 crystalline domains compared with neat Pebax. The high tendency of fillers to the PA-6 and PEO domains and their interference with crystalline domains leads to a more amorphous polymer structure (see XRD results and Table 1). Besides, the melting temperature of PA-6 segments gradually decreased with the increase of filler concentrations, reaching 184.1 °C at 9 wt % His-NPs content due to perturbation of hydrogen-bonding in the Pebax hard segments.

The lower crystallinity of the Pebax soft domains reduces the overall chain rigidity of the PEO chains and results in reduced T_g and loss of the mechanical properties in the MMMs at low filler concentrations, *i.e.*, 0.6 wt %. On the other hand, at higher filler loadings, the hydrogen-bonding interactions between His-NPs and the Pebax chains rigidify the polymer matrix. Also, His-NPs further pull hard domains into the soft segments, thereby

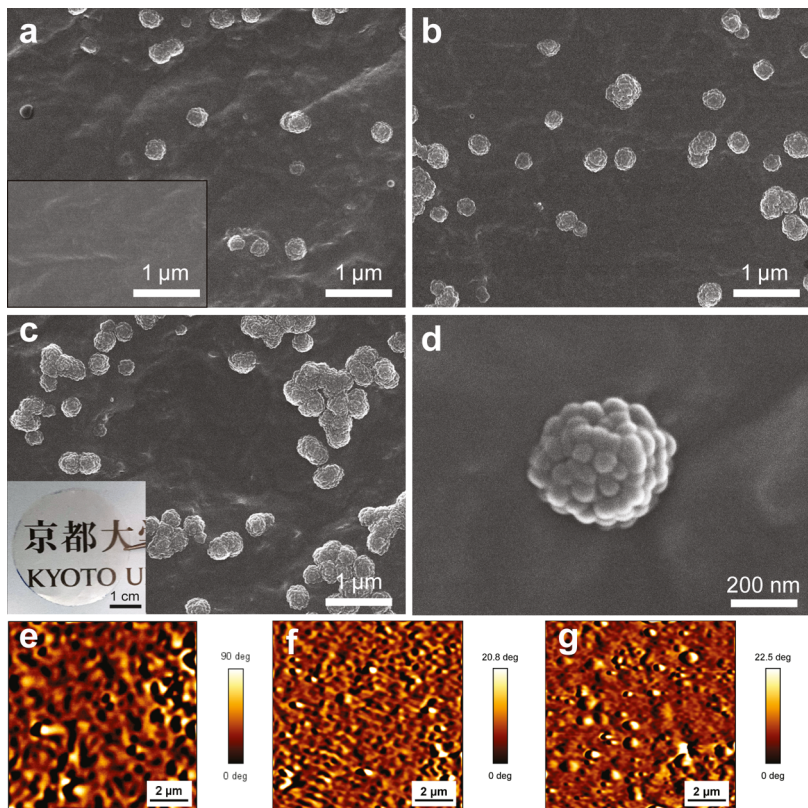


Figure 7. FESEM cross-section images of membranes at different His-NP filler loadings. (a) 0.6 wt % (inset shows neat Pebax film), (b) 3 wt %, and (c) 9 wt % (inset is the photo of MMM with 9 wt % His-NPs). (d) Higher magnification of the filler inside the Pebax matrix. AFM phase images of (e) neat Pebax and nanocomposite membranes with (f) 3 wt % and (g) 9 wt % His-NP loadings.

rigidifying the polymer matrix and shifting the T_g to higher values.

We evaluated the thermal stability of the membranes using the TGA technique. The TGA–DTG curves of neat Pebax, His-NP particles, and representative MMMs are presented in Figure 6b,c. Neat Pebax film showed a one-step decomposition between 320 and 440 °C due to the polymer backbone's chain scission and thermal degradation.³⁶ On the other hand, a two-stage weight loss was observed in the His-NP-loaded membranes due to the degradation of fillers and polymer matrix. The thermal degradation of the organic precursor in His-NPs occurs between 250–340 °C following the initial evaporation of the adsorbed water at above 100 °C. The Pebax/His-NPs MMMs onset weight loss temperatures were higher than the degradation temperature of the filler itself (Figure S4), demonstrating an interaction between Pebax and His-NPs as discussed in the FTIR section. MMMs generally showed lower decomposition temperatures than neat Pebax due to the lower inherent thermal stability of the filler. Nevertheless, considering either the onset of decomposition temperature or the highest weight loss step, the overall thermal stability of the membranes is still sufficiently high for CO₂ capture applications.

The nanoindentation-based mechanical analyses of neat Pebax and representative MMMs are depicted in Figures 6d and S7. The inclusion of small amounts of His-NPs, e.g., 0.6 wt %, into the Pebax matrix decreases Young's modulus and hardness of the membranes due to the reduction in the crystallinity of the polymer matrix (aligned with the XRD and DSC results described above). With further increase in the filler content up to 9 wt %, however, both Young's modulus and hardness of the membranes improved and reached 193 and

197% of their initial values, respectively. The superior mechanical properties of the His-NP-based membranes are associated with the strong hydrogen-bonding interactions at the polymer-filler interfaces and (Pebax) chain rigidification, as observed as an increase in T_g of PEO segments of the Pebax matrix.

3.4. Morphological Evaluation of the Membranes. We examined the morphology and phase behaviors of Pebax/His-NP membranes by scanning electron microscopy (SEM) and AFM imaging (Figure 7). The cross-section of the Pebax matrix was dense and smooth without any sign of large defects (inset in Figure 7a). The His-NPs appeared as globular aggregated particles with an average size of ~200–300 nm on the cross-section of the MMMs (Figure 7b–d). The cross-section area became more densely loaded with nanoparticles by increasing the filler's loading. However, even at relatively high loadings, the MMMs showed uniform particle distribution without apparent defect formations at the polymer–filler interface, forming transparent films (inset in Figure 7c). These results confirmed the strong compatibility between the nanozyme particles and the Pebax matrix, which is required to achieve highly efficient gas separation membranes free of nonselective voids.

The random distribution of soft (PEO) and hard (PA-6) domains in the Pebax structure led to a microphase-separated morphology as observed by AFM. Color profiles of phase images display the differences between hard and soft domains, with darker and lighter hues corresponding to hard and soft regions,⁴² respectively (Figure 7e). Upon adding His-NPs to the Pebax, the spherical nanoparticles appeared on the surface of membranes, and the microphase mixing of the polymer matrix improved (Figure 7f,g).

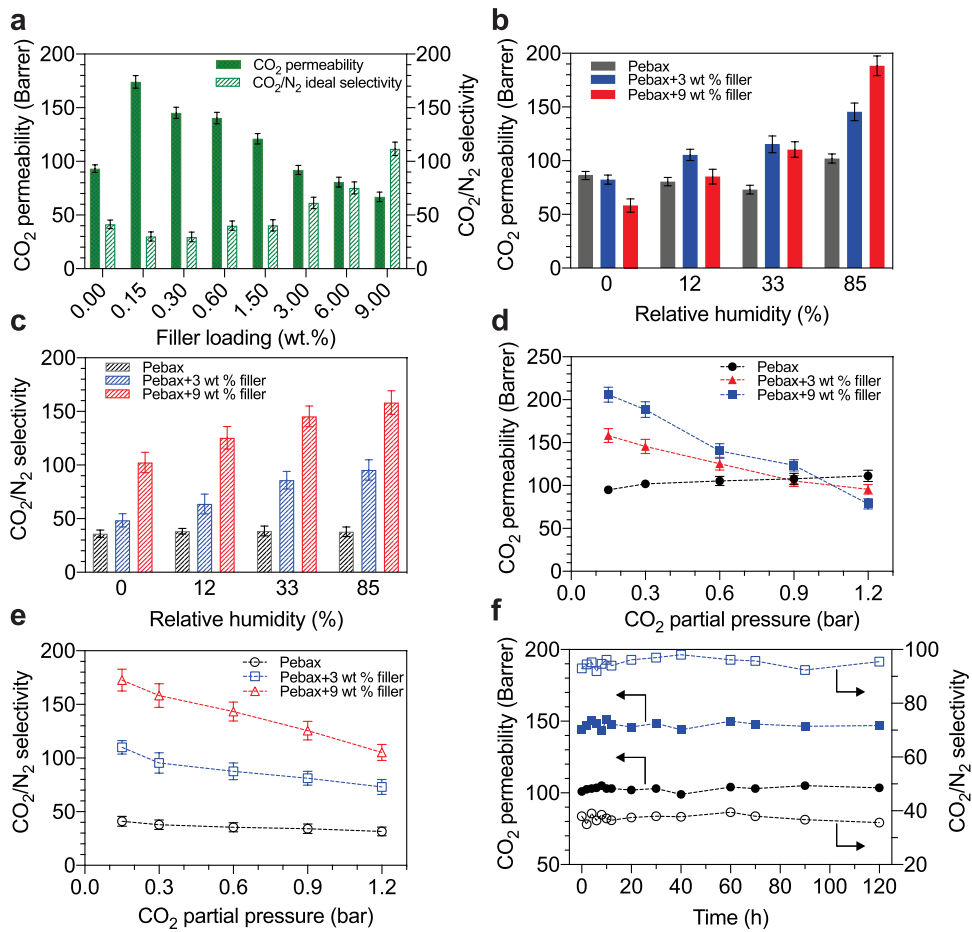


Figure 8. (a) CO₂ permeability and CO₂/N₂ ideal selectivity of neat Pebax membrane and His-NP-containing MMMs at different filler loadings. Effect of humidity on (b) CO₂ permeability and (c) CO₂/N₂ selectivity of the membranes. The feed was dry and humid mixed gas (15/85 vol % CO₂/N₂) at 25 °C and 2 bar. Effect of pressure on (d) CO₂ permeability and (e) CO₂/N₂ selectivity of the membranes. The feed was humid (85% RH) mixed gas (15/85 vol % CO₂/N₂ gas mixture) at 25 °C. (f) Separation performance of Pebax (black circles) and MMM with 3 wt %. His-NPs filler (blue square) under continuous humid (85% RH) mixed gas (15/85 vol % CO₂/N₂ gas mixture) at 25 °C and 2 bar.

Previously, we demonstrated that adding organic–inorganic nanofillers to PEO-based copolymers could alter the crystallinity, the soft–hard domain interactions, and the degree of phase separation in the polymer matrix.⁴⁰ The His-NP nanofillers interact with both soft and hard domains of the Pebax *via* hydrogen-bonding (FTIR analysis). Because of these interactions, nanoparticles could act as crosslinking points⁴³ between the hard and soft domains, constraining chain mobility (as manifested by higher T_g values in DSC thermograms) and, thus, limiting the degree of microphase separation. This outcome is also evident in AFM images, as the hard and soft domains exhibit a lower degree of phase difference.

3.5. Gas Transport Properties. We performed comprehensive gas transport tests to study the effect of His-NPs on the membrane separation performances. Figure 8a summarizes the CO₂ permeability and ideal CO₂/N₂ selectivity of MMMs comprising various loadings of His-NPs. In agreement with a previous report,⁴⁴ neat Pebax membranes had a CO₂ permeability and an ideal CO₂/N₂ selectivity of ~93 Barrer and ~41, respectively.

Upon the addition of His-NPs, the CO₂ permeability of resulting MMMs improved initially to ~174 Barrer but gradually decreased with increasing His-NP loading. On the other hand, at low filler loadings, *i.e.*, 0.15 and 0.3 wt %, the CO₂/N₂ ideal selectivity reduced slightly. Then, it increased steadily with the

filler content, peaking around 110, almost 2.6 times the level of neat Pebax membrane.

The initial increase in CO₂ permeability at low filler concentrations is likely caused by interference of His-NPs in the crystallization of Pebax, as evidenced by XRD and DSC observations. Incorporating His-NPs and their interactions with the polymer matrix disrupt the hard segment crystallinity and reduce chain packing in Pebax, thereby providing more free volume and improving the gas transport performance of MMMs. However, with a further increase in the filler content, a higher amount of dense His-NP locates in the soft domains, obstructing gas transport paths with an increase in tortuosity and polymer rigidification, consequently reducing gas permeability. On another note, the polymer matrix becomes more phase-mixed at higher filler loadings, as confirmed by AFM imaging (Figure 7e–g). Therefore, the soft parts become less permeable to the gas molecules.⁴⁵

The tortuous pathways will likely increase the diffusion restrictions for large gas molecules such as N₂ while permitting the diffusion of small molecules, such as CO₂, thus improving CO₂/N₂ selectivity. In addition, the presence of Zn²⁺ and polar functional groups, such as carboxylic and imidazole moieties, in the structure of His-NPs contributes to a higher solubility for CO₂ and further enhances the CO₂/N₂ selectivity of membranes (Table 2).

Table 2. CO₂ and N₂ Diffusivity and Solubility Coefficients of Pebax and Pebax/His-NPs MMMs

membrane	D _{CO₂} ^a	D _{N₂} ^a	S _{CO₂} ^b	S _{N₂} ^b
Pebax	3.94 ± 0.24	2.86 ± 0.21	23.65 ± 2.3	0.79 ± 0.06
0.6 wt % His-NPs	3.81 ± 0.25	2.60 ± 0.20	36.85 ± 2.5	1.35 ± 0.11
3 wt % His-NPs	2.20 ± 0.16	0.95 ± 0.11	41.82 ± 3.1	1.58 ± 0.12
9 wt % His-NPs	1.42 ± 0.12	0.33 ± 0.05	47.18 ± 3.4	1.82 ± 0.12

^aDiffusivity coefficient: ×10⁻⁷ [cm² s⁻¹]. ^bSolubility coefficient: ×10⁻³ [cm³(STP) cm⁻³ cm Hg⁻¹].

Pebax membrane and representative MMMs were also tested with a 15/85 vol % CO₂/N₂ gas mixture close to flue gas composition to investigate their separation performance under binary CO₂ feeds. In general, CO₂ permeability and CO₂/N₂ selectivity obtained from the dried mixed-gas measurements were slightly lower than those measured for single-gas due to the competitive sorption of the gas molecules.⁴⁶ For example, CO₂ permeability and CO₂/N₂ selectivity of Pebax membrane decreased ~9 and ~18%, respectively (Figure 8b). Also, the CO₂/N₂ selectivity of MMMs with 3 and 9 wt % His-NPs decreased by 13 and 6%, respectively (Figure 8c). Flue gas streams always contain a significant amount of water, irrespective of the source.⁴⁷ Thus, the prepared membranes were tested against humid mixed feeds to evaluate their potential for post-combustion CO₂ capture. The gas separation properties of Pebax change depending on the relative humidity (RH) of the feed gas owing to its hydrophilic nature.⁴⁸

When the neat Pebax membrane is exposed to a humid-gas mixture, its CO₂ permeability (86.2 Barrer under dry conditions) falls to 80.5 and 73.1 Barrer at 12 and 33% RH, respectively, and then increases to 105.6 Barrer at 85% RH. Conversely, CO₂/N₂ selectivity exhibited an opposite trend while remaining higher at 85% RH than in dry conditions. Initially, the water vapor fills up the free volume of the polymer matrix and decreases the gas permeability. However, as humidity rises, the Pebax structure swells, and gas flux increases. Water molecules present in the polymer matrix also facilitate CO₂ solubility, increasing CO₂ permeability and CO₂/N₂ selectivity simultaneously.

Nevertheless, when His-NP-based MMMs were tested with a humid CO₂ mixture, the separation performance of the membranes behaved differently from neat Pebax. Overall, the humidity has a more noticeable impact on the separation performance of MMMs. For example, at 85% RH, the CO₂/N₂ selectivity increased to almost twice and 1.5 times its original value under dry conditions in the samples with 3 and 9 wt % fillers, respectively.

The superior performance of MMMs under humid-gas feeds can be explained by the alteration of the chemical micro-environments of CO₂ molecules in the presence of His-NPs inside the polymer matrix. His-NPs not only improve the dissolution but also facilitate the transport of CO₂ molecules in humid conditions.

In membrane gas separation technology, humidity often poses a great challenge.⁴⁹ For the membrane design proposed in this work, however, the humid-gas feed supplies the required free hydroxyl (OH⁻) ions through the autoionization of water molecules (eqs 6 and 7)



Because of the hydrophilic segments in the Pebax structure, OH⁻ ions become available within the membrane structure. And thus, CO₂ molecules encounter OH⁻ ions in the presence of CA-mimicking His-NPs, giving rise to bicarbonate ions (HCO₃⁻).

The HCO₃⁻ ions will permeate faster through the hydrated pathways of membranes than plain gas molecules through solid polymers, enhancing the overall mass transport inside the polymer matrix. If the membrane transport pathways become fully hydrated, assuming the full connectivity of transport pathways, HCO₃⁻ ions are likely to diffuse at a similar rate to HCO₃⁻ molecules in water. According to the literature,⁵⁰ the diffusion coefficient of bicarbonate ions through the water at room temperature is in the range of 10⁻⁵ cm² s⁻¹, which is about 2 orders of magnitude higher than the diffusion coefficient of the gas molecules in polymer membranes (~10⁻⁷ cm² s⁻¹). Besides, the functional groups, *i.e.*, carboxylic, imidazole, and amines, on the surface of His-NPs interact with CO₂ and water molecules, enhancing the CO₂ solubility and gas transport following the solution-diffusion mechanism.

The effect of pressure on the gas separation performances of neat Pebax and His-NP-based MMMs was tested using humid mixed gas (15/85 v/v % CO₂/N₂ gas mixture) in the range of 1–8 bar (Figure 8e). Despite the slight change in permeability and selectivity of neat Pebax membrane due to the coupling effect and induced plasticization under high pressures, both CO₂ permeability and CO₂/N₂ selectivity of MMMs were significantly reduced as pressure increased. This could be explained by the high solubility of CO₂ molecules and the saturation of His-NPs' active sites at high CO₂ pressures, as observed in other facilitated transport systems.⁵¹ Furthermore, the reduction of separation performance was enhanced with the increase in filler loading. For example, by increasing the partial pressure of CO₂ to 1.2 bar (feed pressure of 8 bar), the CO₂ permeability and CO₂/N₂ selectivity of the membrane with 3 wt % His-NPs were reduced by 40 and 34%, while in the membrane with 9 wt % His-NPs these values decreased to 62 and 39%, respectively.

The long-term stability of membranes is crucial for their practical applications. A representative MMM with 3 wt % His-NPs was tested under continuous humid (85% RH) gas feed (15/85 v/v %) at 2 bar and 25 °C for 120 h (Figure 8f). The MMM demonstrated stable separation performance close to the original values without any signs of deterioration during the testing period, confirming the reversible interactions between the enzyme-mimicking carriers, water, and CO₂ molecules.

The CO₂/N₂ separation performance of the His-NP-based MMMs was compared with Robeson's upper bound (2008) and representative Pebax-based MMMs in the literature (Figure 7 and Table S2). Under dry conditions, incorporating His-NPs into the Pebax matrix brings the performance close to the upper bound by enhancing the CO₂/N₂ selectivity. In humid-gas feed, the performance improvement is more profound, significantly increasing CO₂ permeability and CO₂/N₂ selectivity. The CO₂ separation performance of our best-performing MMM designs surpassed Robeson's upper bound (2008), further revealing the potential of enzyme-mimic fillers for developing highly efficient CO₂ capture membranes (Figure 9).

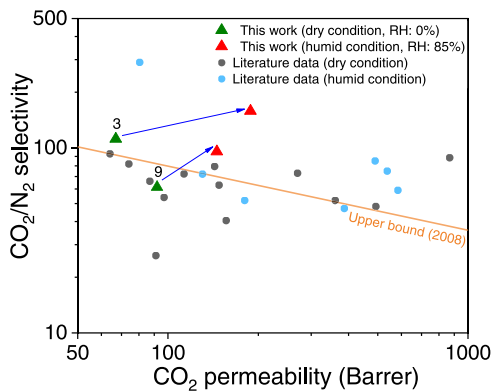


Figure 9. CO₂ separation performance of representative His-NP-based MMMs compared to Robeson's upper bound (2008). Green triangles are representative His-NP-based membranes tested with dry single-gases. The numbers on the top of the markers indicate the weight percentage of His-NP fillers in the membranes. Red triangles are data related to the same membranes tested with humid-gas feeds (85% RH). Gray (dry feeds) and blue (humid feeds) circles represent the reported state-of-the-art Pebax-based MMMs in the literature. The full list of the literature data with references is presented in Table S2.

4. CONCLUSIONS

Here, we report the design of a high-performance nanocomposite membrane for CO₂ separation using zinc-coordinated histidine-based bolaamphiphile assemblies as functional nanofillers. We showed that the bolaamphiphiles could express CA-like active sites (zinc-imidazole and -carboxylate complexes) suitable to serve as transport facilitators. By varying the amount of zinc ions, we could modulate the catalytic activity of the resulting nanoassemblies. And using the *p*NPA assay, we were able to determine an optimum zinc concentration for coordination. Based on morphological, spectroscopic, and thermal analyses, the bolaamphiphilic nanofillers, which are rich in organic moieties, could give defect-free nanocomposite membranes. Our results suggested that the hydrogen-bonding interactions are the driving force of nanofiller–matrix compatibility. Crucially, the nanofillers could only improve the gas solubility of the polymer matrix under dry conditions; however, their CA-mimicking nature manifested itself under humid conditions, facilitating the CO₂ transport. As a result, our membrane design demonstrated exceptionally high CO₂/N₂ selectivity (up to 158.2) and CO₂ permeability (up to 188.4), exceeding Robeson's 2008 upper bound.

ASSOCIATED CONTENT

Supporting Information

The Supporting Information is available free of charge at <https://pubs.acs.org/doi/10.1021/acsami.2c06270>.

Catalytic activity measurements; ¹H NMR spectra of His-Bola molecules; DLS analysis of His-Bola assemblies; C 1s XPS spectrum of His-NPs; TGA analysis of His-Bola and His-NPs; pH decay experiment; UV-vis spectra of solutions with His-NPs at different pH values; and *P-h* curves of nanoindentation measurements ([PDF](#))

AUTHOR INFORMATION

Corresponding Authors

Easan Sivaniah – Institute for Integrated Cell-Material Sciences (iCeMS), Kyoto University, 606-8501 Kyoto, Japan; Department of Molecular Engineering, Graduate School of

Engineering, Kyoto University, 615-8510 Kyoto, Japan;

Email: esivaniah@icems.kyoto-u.ac.jp

Behnam Ghalei – Institute for Integrated Cell-Material Sciences (iCeMS), Kyoto University, 606-8501 Kyoto, Japan; Department of Molecular Engineering, Graduate School of Engineering, Kyoto University, 615-8510 Kyoto, Japan; orcid.org/0000-0003-2848-9138; Email: bghalei@icems.kyoto-u.ac.jp

Authors

Somaye Nilouyal – Institute for Integrated Cell-Material Sciences (iCeMS), Kyoto University, 606-8501 Kyoto, Japan; Department of Molecular Engineering, Graduate School of Engineering, Kyoto University, 615-8510 Kyoto, Japan

H. Enis Karahan – Institute for Integrated Cell-Material Sciences (iCeMS), Kyoto University, 606-8501 Kyoto, Japan; Department of Molecular Engineering, Graduate School of Engineering, Kyoto University, 615-8510 Kyoto, Japan; Synthetic Fuels & Chemicals Technology Center (ITU-SENTEK), Istanbul Technical University, 34469 Istanbul, Turkey; orcid.org/0000-0002-7753-1024

Ali Pournaghshband Isfahani – Institute for Integrated Cell-Material Sciences (iCeMS), Kyoto University, 606-8501 Kyoto, Japan; Department of Molecular Engineering, Graduate School of Engineering, Kyoto University, 615-8510 Kyoto, Japan; orcid.org/0000-0001-5188-385X

Daisuke Yamaguchi – Institute for Integrated Cell-Material Sciences (iCeMS), Kyoto University, 606-8501 Kyoto, Japan; Department of Molecular Engineering, Graduate School of Engineering, Kyoto University, 615-8510 Kyoto, Japan; orcid.org/0000-0001-9643-4513

Andrew H. Gibbons – Institute for Integrated Cell-Material Sciences (iCeMS), Kyoto University, 606-8501 Kyoto, Japan; Department of Molecular Engineering, Graduate School of Engineering, Kyoto University, 615-8510 Kyoto, Japan

Masateru M. M. Ito – Institute for Integrated Cell-Material Sciences (iCeMS), Kyoto University, 606-8501 Kyoto, Japan; Department of Molecular Engineering, Graduate School of Engineering, Kyoto University, 615-8510 Kyoto, Japan

Complete contact information is available at: <https://pubs.acs.org/10.1021/acsami.2c06270>

Author Contributions

S.N. and B.G. conceived the research idea. S.N. and B.G. designed the study with the input of E.S. and H.E.K. S.N. performed the majority of experimental work and prepared the original draft. B.G. and H.E.K. carried out manuscript review and editing. H.E.K., A.P.I., D.Y., A.H.G., and M.M.I. supported the data analysis. B.G. and E.S. made supervision. All authors discussed the results and contributed to manuscript refinement.

Notes

The authors declare no competing financial interest.

ACKNOWLEDGMENTS

B.G. gratefully acknowledges the Japan Society for the Promotion of Science (JSPS) for KAKENHI funding (grant numbers: 18K14042 and 22K04873). E.S. acknowledges JSPS for KAKENHI funding (grant number: 20H00390). This work was supported by the central facilities and analysis center at iCeMS, KUIAS, Kyoto University. H.E.K. acknowledges the funding support of the JSPS under the JSPS International Fellowship program and The Scientific and Technological

Research Council of Turkey (TÜBİTAK) under the BIDEB 2221 visiting fellowship program.

■ REFERENCES

- (1) Svitiski, J.; Waters, C. N.; Day, J.; Milliman, J. D.; Summerhayes, C.; Steffen, W.; Zalasiewicz, J.; Cearreta, A.; Galuszka, A.; Hajdas, I.; Head, M. J.; Leinfelder, R.; McNeill, J. R.; Poirier, C.; Rose, N. L.; Shotyk, W.; Wagreich, M.; Williams, M. Extraordinary Human Energy Consumption and Resultant Geological Impacts Beginning around 1950 CE Initiated the Proposed Anthropocene Epoch. *Commun. Earth Environ.* **2020**, *1*, No. 32.
- (2) Milani, D.; Kiani, A.; McNaughton, R. Renewable-Powered Hydrogen Economy from Australia's Perspective. *Int. J. Hydrogen Energy* **2020**, *45*, 24125–24145.
- (3) Razmjoo, A.; Kaigutha, L. G.; Rad, M. A. V.; Marzband, M.; Davarpanah, A.; Denai, M. A Technical Analysis Investigating Energy Sustainability Utilizing Reliable Renewable Energy Sources to Reduce CO₂ Emissions in a High Potential Area. *Renewable Energy* **2021**, *164*, 46–57.
- (4) Yalcin, S.; Konukman, A. E. S.; Midilli, A. A Perspective on Fossil Fuel Based Flue Gas Emission Reduction Technologies. *Greenhouse Gases: Sci. Technol.* **2020**, *10*, 664–677.
- (5) Siagian, U. W. R.; Raksaati, A.; Himma, N. F.; Khoiruddin, K.; Wenten, I. G. Membrane-Based Carbon Capture Technologies: Membrane Gas Separation vs. Membrane Contactor. *J. Nat. Gas Sci. Eng.* **2019**, *67*, 172–195.
- (6) Park, H. B.; Kamcev, J.; Robeson, L. M.; Elimelech, M.; Freeman, B. D. Maximizing the Right Stuff: The Trade-off between Membrane Permeability and Selectivity. *Science* **2017**, *356*, No. eaab0530.
- (7) Wang, S.; Li, X.; Wu, H.; Tian, Z.; Xin, Q.; He, G.; Peng, D.; Chen, S.; Yin, Y.; Jiang, Z.; Guiver, M. D. Advances in High Permeability Polymer-Based Membrane Materials for CO₂ Separations. *Energy Environ. Sci.* **2016**, *9*, 1863–1890.
- (8) Wang, S.; Wu, Y.; Zhang, N.; He, G.; Xin, Q.; Wu, X.; Wu, H.; Cao, X.; Guiver, M. D.; Jiang, Z. A Highly Permeable Graphene Oxide Membrane with Fast and Selective Transport Nanochannels for Efficient Carbon Capture. *Energy Environ. Sci.* **2016**, *9*, 3107–3112.
- (9) Isfahani, A. P.; Ghalei, B.; Wakimoto, K.; Bagheri, R.; Sivaniah, E.; Sadeghi, M. Plasticization Resistant Crosslinked Polyurethane Gas Separation Membranes. *J. Mater. Chem. A* **2016**, *4*, 17431–17439.
- (10) Gouveia, A. S. L.; Bumenn, E.; Rohtlaid, K.; Michaud, A.; Vieira, T. M.; Alves, V. D.; Tomé, L. C.; Plesse, C.; Marrucho, I. M. Ionic Liquid-Based Semi-Interpenetrating Polymer Network (SIPN) Membranes for CO₂ Separation. *Sep. Purif. Technol.* **2021**, *274*, No. 118437.
- (11) Lv, X.; Huang, L.; Ding, S.; Wang, J.; Li, L.; Liang, C.; Li, X. Mixed Matrix Membranes Comprising Dual-Facilitated Bio-Inspired Filler for Enhancing CO₂ Separation. *Sep. Purif. Technol.* **2021**, *276*, No. 119347.
- (12) Rea, R.; De Angelis, M. G.; Baschetti, M. G. Models for Facilitated Transport Membranes: A Review. *Membranes* **2019**, *9*, No. 26.
- (13) Lee, Y.-Y.; Gurkan, B. Graphene Oxide Reinforced Facilitated Transport Membrane with Poly (Ionic Liquid) and Ionic Liquid Carriers for CO₂/N₂ Separation. *J. Membr. Sci.* **2021**, *638*, No. 119652.
- (14) Ren, S.; Li, C.; Tan, Z.; Hou, Y.; Jia, S.; Cui, J. Carbonic Anhydrase@ ZIF-8 Hydrogel Composite Membrane with Improved Recycling and Stability for Efficient CO₂ Capture. *J. Agric. Food Chem.* **2019**, *67*, 3372–3379.
- (15) Sun, J.; Wang, C.; Wang, Y.; Ji, S.; Liu, W. Immobilization of Carbonic Anhydrase on Polyethylenimine/Dopamine Codeposited Membranes. *J. Appl. Polym. Sci.* **2019**, *136*, No. 47784.
- (16) Bednár, A.; Nemestóthy, N.; Bakonyi, P.; Fülöp, L.; Zhen, G.; Lu, X.; Kobayashi, T.; Kumar, G.; Xu, K.; Bélaifi-Bakó, K. Enzymatically-Boosted Ionic Liquid Gas Separation Membranes Using Carbonic Anhydrase of Biomass Origin. *Chem. Eng. J.* **2016**, *303*, 621–626.
- (17) Robinson, P. K. Enzymes: Principles and Biotechnological Applications. *Essays Biochem.* **2015**, *59*, 1–41.
- (18) Molina-Fernández, C.; Luis, P. Immobilization of Carbonic Anhydrase for CO₂ Capture and Its Industrial Implementation: A Review. *J. CO₂ Util.* **2021**, *47*, No. 101475.
- (19) Prabhu, C.; Valechha, A.; Wanjari, S.; Labhsetwar, N.; Kotwal, S.; Satyanarayanan, T.; Rayalu, S. Carbon Composite Beads for Immobilization of Carbonic Anhydrase. *J. Mol. Catal. B: Enzym.* **2011**, *71*, 71–78.
- (20) Zhang, Y.; Wang, H.; Zhou, S.; Wang, J.; He, X.; Liu, J.; Zhang, Y. Biomimetic Material Functionalized Mixed Matrix Membranes for Enhanced Carbon Dioxide Capture. *J. Mater. Chem. A* **2018**, *6*, 15585–15592.
- (21) Saeed, M.; Deng, L. CO₂ Facilitated Transport Membrane Promoted by Mimic Enzyme. *J. Membr. Sci.* **2015**, *494*, 196–204.
- (22) Wang, Z.; Zhang, Y.; Wang, J.; Zhang, Y. Bioinspired Porous Organic Polymer-Functionalized Membranes for Efficient CO₂ Capture. *Sustainable Energy Fuels* **2020**, *4*, 1191–1198.
- (23) Zheng, W.; Tian, Z.; Wang, Z.; Peng, D.; Zhang, Y.; Wang, J.; Zhang, Y. Dual-Function Biomimetic Carrier Based Facilitated Transport Mixed Matrix Membranes with High Stability for Efficient CO₂/N₂ Separation. *Sep. Purif. Technol.* **2022**, *285*, No. 120371.
- (24) Jones, J. H.; Wood, M. E. L-Histidine Benzyl Ester. *Synth. Commun.* **1986**, *16*, 1515–1516.
- (25) Kim, M.; Lee, S. Carbonic Anhydrase-Mimetic Bolaamphiphile Self-Assembly for CO₂ Hydration and Sequestration. *Chem. - Eur. J.* **2014**, *20*, 17019–17024.
- (26) Clarizia, G.; Bernardo, P.; Gorras, G.; Zampino, D.; Carroccio, S. C. Influence of the Preparation Method and Photo-Oxidation Treatment on the Thermal and Gas Transport Properties of Dense Films Based on a Poly (Ether-Block-Amide) Copolymer. *Materials* **2018**, *11*, No. 1326.
- (27) Huang, Y.; Zhang, S.; Chen, H.; Zhao, L.; Zhang, Z.; Cheng, P.; Chen, Y. A Zinc Coordination Complex Mimicking Carbonic Anhydrase for CO₂ Hydrolysis and Sequestration. *Inorg. Chem.* **2019**, *58*, 9916–9921.
- (28) Keum, C.; Cho, J.; Park, S.; Lee, S. Y. Copper-Coordinated Histidyl Bolaamphiphile Assembly as an Oxidative Catalyst: Coordination Structure and Catalytic Activity in Cyclohexane Oxidation. *ChemCatChem* **2019**, *11*, 4935–4943.
- (29) Edington, S. C.; Gonzalez, A.; Middendorf, T. R.; Halling, D. B.; Aldrich, R. W.; Baiz, C. R. Coordination to Lanthanide Ions Distorts Binding Site Conformation in Calmodulin. *Proc. Natl. Acad. Sci. U.S.A.* **2018**, *115*, E3126–E3134.
- (30) Keum, C.; Lee, S. Iridium-Coordinated Histidyl Bolaamphiphile Self-Assemblies as Heterogeneous Catalysts for Water Oxidation. *ChemSusChem* **2018**, *11*, 2569–2578.
- (31) Feyer, V.; Plekan, O.; Tsud, N.; Cháb, V.; Matolín, V.; Prince, K. C. Adsorption of Histidine and Histidine-Containing Peptides on Au (111). *Langmuir* **2010**, *26*, 8606–8613.
- (32) Tian, F.; Cerro, A. M.; Mosier, A. M.; Wayment-Steele, H. K.; Shine, R. S.; Park, A.; Webster, E. R.; Johnson, L. E.; Johal, M. S.; Benz, L. Surface and Stability Characterization of a Nanoporous ZIF-8 Thin Film. *J. Phys. Chem. C* **2014**, *118*, 14449–14456.
- (33) Liang, S.; Wu, X.-L.; Zong, M.-H.; Lou, W.-Y. Zn-Triazole Coordination Polymers: Bioinspired Carbonic Anhydrase Mimics for Hydration and Sequestration of CO₂. *Chem. Eng. J.* **2020**, *398*, No. 125530.
- (34) Peng, C.; Crawshaw, J. P.; Maitland, G. C.; Trusler, J. P. M.; Vega-Maza, D. The PH of CO₂-Saturated Water at Temperatures between 308 K and 423 K at Pressures up to 15 MPa. *J. Supercrit. Fluids* **2013**, *82*, 129–137.
- (35) Thanakkasarane, S.; Kim, D.; Seo, J. Preparation and Characterization of Poly (Ether-Block-Amide)/Polyethylene Glycol Composite Films with Temperature-Dependent Permeation. *Polymers* **2018**, *10*, No. 225.
- (36) Huang, G.; Isfahani, A. P.; Muchtar, A.; Sakurai, K.; Shrestha, B. B.; Qin, D.; Yamaguchi, D.; Sivaniah, E.; Ghalei, B. Pebax/Ionic Liquid Modified Graphene Oxide Mixed Matrix Membranes for Enhanced CO₂ Capture. *J. Membr. Sci.* **2018**, *565*, 370–379.

- (37) Bernardo, P.; Clarizia, G. Enhancing Gas Permeation Properties of Pebax 1657 Membranes via Polysorbate Nonionic Surfactants Doping. *Polymers* **2020**, *12*, No. 253.
- (38) Kamal, T.; Park, S.-Y.; Choi, M.-C.; Chang, Y.-W.; Chuang, W.-T.; Jeng, U.-S. An In-Situ Simultaneous SAXS and WAXS Survey of PEBAK Nanocomposites Reinforced with Organoclay and POSS during Uniaxial Deformation. *Polymer* **2012**, *53*, 3360–3367.
- (39) Dal Pont, K.; Serghei, A.; Espuche, E. Multifunctional Pd-Based Nanocomposites with Designed Structure from In Situ Growth of Pd Nanoparticles and Polyether Block Amide Copolymer. *Polymers* **2021**, *13*, No. 1477.
- (40) Isfahani, A. P.; Sadeghi, M.; Nilouyal, S.; Huang, G.; Muchtar, A.; Ito, M. M.; Yamaguchi, D.; Sivaniah, E.; Ghalei, B. Tuning the Morphology of Segmented Block Copolymers with Zr-MOF Nanoparticles for Durable and Efficient Hydrocarbon Separation Membranes. *J. Mater. Chem. A* **2020**, *8*, 9382–9391.
- (41) Meshkat, S.; Kaliaguine, S.; Rodrigue, D. Comparison between ZIF-67 and ZIF-8 in Pebax MH-1657 Mixed Matrix Membranes for CO₂ Separation. *Sep. Purif. Technol.* **2020**, *235*, No. 116150.
- (42) Isfahani, A. P.; Shahrooz, M.; Yamamoto, T.; Muchtar, A.; Ito, M. M.; Yamaguchi, D.; Takenaka, M.; Sivaniah, E.; Ghalei, B. Influence of Microstructural Variations on Morphology and Separation Properties of Polybutadiene-Based Polyurethanes. *RSC Adv.* **2021**, *11*, 15449–15456.
- (43) Zheng, J.; Ozisik, R.; Siegel, R. W. Disruption of Self-Assembly and Altered Mechanical Behavior in Polyurethane/Zinc Oxide Nanocomposites. *Polymer* **2005**, *46*, 10873–10882.
- (44) Embaye, A. S.; Martínez-Izquierdo, L.; Malankowska, M.; Téllez, C.; Coronas, J. Poly(Ether-Block-Amide) Copolymer Membranes in CO₂ Separation Applications. *Energy Fuels* **2021**, *35*, 17085–17102.
- (45) Isfahani, A. P.; Ghalei, B.; Bagheri, R.; Kinoshita, Y.; Kitagawa, H.; Sivaniah, E.; Sadeghi, M. Polyurethane Gas Separation Membranes with Ethereal Bonds in the Hard Segments. *J. Membr. Sci.* **2016**, *513*, 58–66.
- (46) Wang, Y.; Li, H.; Dong, G.; Scholes, C.; Chen, V. Effect of Fabrication and Operation Conditions on CO₂ Separation Performance of PEO-PA Block Copolymer Membranes. *Ind. Eng. Chem. Res.* **2015**, *54*, 7273–7283.
- (47) Shi, Z.; Tao, Y.; Wu, J.; Zhang, C.; He, H.; Long, L.; Lee, Y.; Li, T.; Zhang, Y.-B. Robust Metal-Triazolate Frameworks for CO₂ Capture from Flue Gas. *J. Am. Chem. Soc.* **2020**, *142*, 2750–2754.
- (48) Deng, J.; Dai, Z.; Hou, J.; Deng, L. Morphologically Tunable MOF Nanosheets in Mixed Matrix Membranes for CO₂ Separation. *Chem. Mater.* **2020**, *32*, 4174–4184.
- (49) Huang, G.; Ghalei, B.; Isfahani, A. P.; Karahan, H. E.; Terada, D.; Qin, D.; Li, C.; Tsujimoto, M.; Yamaguchi, D.; Sugimoto, K.; Igarashi, R.; Chang, B. K.; Li, T.; Shirakawa, M.; Sivaniah, E. Overcoming Humidity-Induced Swelling of Graphene Oxide-Based Hydrogen Membranes Using Charge-Compensating Nanodiamonds. *Nat. Energy* **2021**, *6*, 1176–1187.
- (50) Zeebe, R. E. On the Molecular Diffusion Coefficients of Dissolved CO₂, HCO₃⁻, and CO₃²⁻ and Their Dependence on Isotopic Mass. *Geochim. Cosmochim. Acta* **2011**, *75*, 2483–2498.
- (51) Wang, Y.; Li, L.; Zhang, X.; Li, J.; Wang, J.; Li, N. Polyvinylamine/Amorphous Metakaolin Mixed-Matrix Composite Membranes with Facilitated Transport Carriers for Highly Efficient CO₂/N₂ Separation. *J. Membr. Sci.* **2020**, *599*, No. 117828.

□ Recommended by ACS

Heteronuclear Dual Single-Atom Catalysts for Ambient Conversion of CO₂ from Air to Formate

Shengliang Zhai, Weiqiao Deng, et al.

MARCH 07, 2023

ACS CATALYSIS

READ ▶

Nanobiomineralization of Carbon Dioxide by Molecularly Engineered Metal-Histidine Complex Nanozymes

Somaye Nilouyal, Behnam Ghalei, et al.

FEBRUARY 15, 2023

CHEMISTRY OF MATERIALS

READ ▶

Boosting CO₂ Electroreduction on Bismuth Nanoplates with a Three-Dimensional Nitrogen-Doped Graphene Aerogel Matrix

Xiao-Ting Jing, An-Xiang Yin, et al.

APRIL 14, 2023

ACS APPLIED MATERIALS & INTERFACES

READ ▶

Regulation of the Coordination Structures of Transition Metals on Nitrogen-Doped Carbon Nanotubes for Electrochemical CO₂ Reduction

Yongyong Cao, Xi Li, et al.

NOVEMBER 14, 2022

INORGANIC CHEMISTRY

READ ▶

Get More Suggestions >